
**AFRL-AFOSR-UK-TR-2024-0001**

# Hibernating Turbulence in Boundary-Layer Flows

**Whalley, Richard**
**NEWCASTLE UNIVERSITY**
**KINGSGATE**
**NEWCASTLE-UPON-TYNE, TYNE AND WEAR, NE1 7RU**
**GBR**

**10/23/2023**
**Final Technical Report**



Air Force Research Laboratory
Air Force Office of Scientific Research
European Office of Aerospace Research and Development
Unit 4515 Box 14, APO AE 09421

# REPORT DOCUMENTATION PAGE

**PLEASE DO NOT RETURN YOUR FORM TO THE ABOVE ORGANIZATION.**

| 1. REPORT DATE | 2. REPORT TYPE | 3. DATES COVERED | |
|---|---|---|---|
| 20231023 | Final | START DATE<br>20170901 | END DATE<br>20230228 |

**4. TITLE AND SUBTITLE**
Hibernating Turbulence in Boundary-Layer Flows

| 5a. CONTRACT NUMBER | 5b. GRANT NUMBER | 5c. PROGRAM ELEMENT NUMBER |
|---|---|---|
| | FA9550-17-1-0231 | 61102F |
| **5d. PROJECT NUMBER** | **5e. TASK NUMBER** | **5f. WORK UNIT NUMBER** |
| | | |

**6. AUTHOR(S)**
Richard Whalley

**7. PERFORMING ORGANIZATION NAME(S) AND ADDRESS(ES)**
NEWCASTLE UNIVERSITY
KINGSGATE
NEWCASTLE-UPON-TYNE, TYNE AND WEAR NE1 7RU
GBR

**8. PERFORMING ORGANIZATION REPORT NUMBER**

| 9. SPONSORING/MONITORING AGENCY NAME(S) AND ADDRESS(ES) | 10. SPONSOR/MONITOR'S ACRONYM(S) | 11. SPONSOR/MONITOR'S REPORT NUMBER(S) |
|---|---|---|
| EOARD<br>UNIT 4515<br>APO AE 09421-4515 | AFRL/AFOSR IOE | AFRL-AFOSR-UK-TR-2024-0001 |

**12. DISTRIBUTION/AVAILABILITY STATEMENT**
A Distribution Unlimited: PB Public Release

**13. SUPPLEMENTARY NOTES**

**14. ABSTRACT**
Experiments are presented to characterise low-drag turbulence events, or so-called intervals of hibernating turbulence, which last for a prolonged duration in a zero-pressure gradient flat-plate turbulent boundary-layer flow over a friction Reynolds number range of Re? = 335 to 880 in either a wind tunnel or water flume. The presented experimental data is acquired at a friction Reynolds number several times higher than all previous investigations on hibernating turbulence in channel flows. The spatiotemporal low-drag intermittencies are identified by applying conditional sampling techniques to either simultaneously acquired wall-shear stress and pointwise streamwise and wall-normal Laser Doppler Velocimetry (LDV) data, or simultaneously acquired wall-shear stress and cross-stream stereoscopic particle image velocimetry (SPIV) data. The hibernating turbulence events occur randomly in space and in time in the turbulent boundary-layer flow, with these intrinsic events generating local skin-friction drag values up to 75% lower than the time-averaged mean skin friction. However, these hibernating turbulence events are rare, typically being found in a single location less than 10% of the time depending on the conditional sampling criteria. It is shown that ensemble-averaged streamwise velocity during intervals of hibernating turbulence fall close to the Maximum Drag Reduction Asymptote (MDR) asymptote at wall-normal distance of $y+ < 40$, in excellent agreement with existing experimental and Direct Numerical Simulation (DNS) data on hibernating turbulence in transitional channel flows. Further from the wall, the conditionally sampled streamwise velocity data follows a gradient similar to the classical Prandtl-von Kármán log-law, upshifted by the scaling with the low-drag friction velocity. This suggests, from an ensemble-averaged point of view, that the wall-turbulence during these intervals of low drag loses communication with the wall beyond $y+ > 40$. The SPIV data shows the hibernating turbulence structure in turbulent boundary-layer flows is characterised by a weak near-wall quasi-streamwise counter-rotating vortex pair, which generates upwash and the low-speed and low-stress streak in the near-wall region. These vortical flow structures move chaotically, disappearing and reappearing within the wall-turbulent flow during the low wall-shear stress events. Whilst the mean streamwise velocity appears to bound the hibernating turbulence structure to the near-wall region, the conditionally sampled Reynolds shear stress data shows a reduction across most of the turbulent boundary layer, when scaled with the oncoming free-stream velocity.

**15. SUBJECT TERMS**

| 16. SECURITY CLASSIFICATION OF: | | | 17. LIMITATION OF ABSTRACT | 18. NUMBER OF PAGES |
|---|---|---|---|---|
| a. REPORT | b. ABSTRACT | c. THIS PAGE | | |
| U | U | U | SAR | 2 |

| 19a. NAME OF RESPONSIBLE PERSON | 19b. PHONE NUMBER *(Include area code)* |
|---|---|
| DOUGLAS SMITH | 314 235 6013 |

**Standard Form 298** (Rev.5/2020)
Prescribed by ANSI Std. Z39.18

# Hibernating Turbulence in Boundary-Layer Flows

**FA9550-17-1-0231**

**Dr Richard D. Whalley**
School of Engineering
Newcastle University
Newcastle, NE1 7RU
United Kingdom

Richard.Whalley@newcastle.ac.uk
www.experimental-fluid-dynamics.com

**Summary**
Experiments are presented to characterise low-drag turbulence events, or so-called intervals of hibernating turbulence, which last for a prolonged duration in a zero-pressure gradient flat-plate turbulent boundary-layer flow over a friction Reynolds number range of $Re_\tau$ = 335 to 880 in either a wind tunnel or water flume. The presented experimental data is acquired at a friction Reynolds number several times higher than all previous investigations on hibernating turbulence in channel flows. The spatiotemporal low-drag intermittencies are identified by applying conditional sampling techniques to either simultaneously acquired wall-shear stress and pointwise streamwise and wall-normal Laser Doppler Velocimetry (LDV) data, or simultaneously acquired wall-shear stress and cross-stream stereoscopic particle image velocimetry (SPIV) data. The hibernating turbulence events occur randomly in space and in time in the turbulent boundary-layer flow, with these intrinsic events generating local skin-friction drag values up to 75% lower than the time-averaged mean skin friction. However, these hibernating turbulence events are rare, typically being found in a single location less than 10% of the time depending on the conditional sampling criteria. It is shown that ensemble-averaged streamwise velocity during intervals of hibernating turbulence fall close to the Maximum Drag Reduction Asymptote (MDR) asymptote at wall-normal distance of $y^+ < 40$, in excellent agreement with existing experimental and Direct Numerical Simulation (DNS) data on hibernating turbulence in transitional channel flows. Further from the wall, the conditionally sampled streamwise velocity data follows a gradient similar to the classical Prandtl-von Kármán log-law, upshifted by the scaling with the low-drag friction velocity. This suggests, from an ensemble-averaged point of view, that the wall-turbulence during these intervals of low drag loses communication with the wall beyond $y^+ > 40$. The SPIV data shows the hibernating turbulence structure in turbulent boundary-layer flows is characterised by a weak near-wall quasi-streamwise counter-rotating vortex pair, which generates upwash and the low-speed and low-stress streak in the near-wall region. These vortical flow structures move chaotically, disappearing and reappearing within the wall-turbulent flow during the low wall-shear stress events. Whilst the mean streamwise velocity appears to bound the hibernating turbulence structure to the near-wall region, the conditionally sampled Reynolds shear stress data shows a reduction across most of the turbulent boundary layer, when scaled with the oncoming free-stream velocity.

**Table of Contents**

**Nomenclature**

| | | |
|---|---|---|
| $x$ | Streamwise distance | m |
| $y$ | Wall-normal distance | m |
| $z$ | Spanwise distance | m |
| $u$ | Fluctuating streamwise velocity | m/s |
| $v$ | Fluctuating wall-normal velocity | m/s |
| $-uv$ | Reynolds shear stress | $m^2/s^2$ |
| $U$ | Absolute streamwise velocity | m/s |
| $U_\infty$ | Free-stream velocity | m/s |
| $V$ | Absolute wall-normal velocity | m/s |
| $u_\tau$ | Friction velocity | m/s |
| $t$ | Time | s |
| $t_f$ | Fraction of time spent in hibernation | s |
| $E$ | Voltage | volts |
| $\rho$ | Density | $kg/m^3$ |
| $\tau$ | Wall-shear stress | Pa |
| $\delta$ | Boundary-layer thickness | m |
| $\upsilon$ | Kinematic viscosity | $m^2/s$ |
| $\lambda$ | Thermal conductivity | W/mK |
| $Re_\tau = \delta.u_\tau/\upsilon$ | Friction Reynolds number | |

**Superscripts**

| | |
|---|---|
| $+$ | Indicates viscous scaling of time, length and velocity, $t^+ = t.u_\tau^2/\upsilon$, $y^+ = yu_\tau/\upsilon$, $u^+ = u/u_\tau$ |
| $*$ | Indicates outer scaling of time, $t^* = t.U_\infty/\delta$ |
| $L$ | Indicates low drag |
| $\overline{U}$ | Overbar indicates a time-averaged or an ensemble-averaged quantity |
| $u'$ | Prime indicates an RMS quantity |

**Prefix**

| | |
|---|---|
| $B(u)$ | Probability density function of $u$ |

**Acronyms**

| | |
|---|---|
| DNS | Direct Numerical Simulation |
| LDV | Laser Doppler Velocimetry |
| SPIV | Stereoscopic Particle Image Velocimetry |
| ECS | Exact Coherent State |
| RMS | Root Mean Square |
| NLR | Non-Linear Regression |
| ADC | Analogue-Digital-Converter |
| MDR | Maximum Drag Reduction |

**List of Figures**

**Introduction**

Turbulent boundary-layer flows can be visualised as a complex entanglement of vortical flow structures[1]. Some of these vortical flow structures extend towards the wall to create cycles of upwash and downwash of turbulent momentum, inducing the classical meandering near-wall streaky flow structure in order to sustain the turbulence flowing over the wall[1–5]. The upwash sides of these vortices create the well-known ejection events, lifting low-speed fluid away from the wall, while simultaneously, the downwash sides of these vortices create the well-known sweep events, pushing high-speed fluid into the wall generating turbulent skin friction. Due to this fluid pumping mechanism, many turbulence control techniques target this near-wall region to disrupt and weaken the near-wall vortical flow structures to reduce the skin-friction drag[6]. Typical approaches have focussed on a change in topography[7,8], low-amplitude wall-normal blowing[9,10], or impositions of spatiotemporal wall-motions[6,11–13]. However, arguably the most successful turbulence control technique is one which can only be used in liquid flows and is the dissolution of rheology-modifying additives to the working fluid[14–16].

Additives can reduce the energy consumption in flow processes by up to 80% and cause a phenomena known as Maximum-Drag-Reduction (MDR)[15]. MDR is an asymptotic upper limit to turbulent drag reduction and its existence is a classical unsolved problem in the turbulent flows of highly drag-reducing polymer solutions. Over the past 20 years, evidence has emerged from low Reynolds number Direct Numerical Simulation (DNS) studies[17–21] that skin-friction drag reduction in polymer solutions is closely connected to weakly turbulent flow structures found in Newtonian fluid flow. In the DNS studies of these polymeric fluid flows, the weakly turbulent flow structures become more apparent as the viscoelasticity suppressed the dominant turbulent motions, revealing spatiotemporal intervals of low drag, which had been noted in much early simulation studies[22]. These intervals of low drag were named “hibernating turbulence.” During intervals of hibernating turbulence, the instantaneous streamwise velocity profile approached the MDR asymptote. As the level of viscoelasticity increased, the frequency of the hibernating turbulence events increased, with the flow cycling in and out of regions of low drag, with a velocity profile which either approached the classical Prandtl-von Kármán log-law or the MDR asymptote. The MDR asymptote appeared as a laminar attractor, with the flow spending time around the MDR asymptote before taking an excursion towards the classical Prandtl-von Kármán log-law, posing an analogy with dynamical system theory[14]. Once the level of viscoelasticity was sufficiently high, the dynamics of the fluid flow changed, generating a sustainable highly-drag reduced fluid flow with a velocity profile which approached the MDR asymptote in a time-averaged sense.

Experimental evidence of hibernating turbulence in transitional channel flows soon followed. Whalley et al.[23,24] showed that the hibernating turbulence flow structure in Newtonian fluid flow resembled a recently discovered travelling wave solution[25]. This presented a possible connection between additive drag reduction, transition-to-turbulence and nontrivial invariant solutions to the Navier-Stokes equations. Over the past 20 years, the mathematical framework of dynamical systems theory has facilitated the significant improvement in physical understanding of transition-to-turbulence in wall-turbulent flows[26–30]. One of the most important discoveries for wall-turbulence was the non-linear travelling wave solutions to the Navier-Stokes equations[26,31–34]. These solutions, or Exact Coherent States (ECS)[35], have allowed a priori investigation of the self-sustaining structures associated with wall-turbulence, which appear as a low-stress streak straddled on either side by a quasi-streamwise counter-rotating vortex pair – similar in appearance to the hibernating turbulence flow structure observed experimentally in low-Reynolds number channel flows[23,24].

More broadly, hibernating turbulence is spatiotemporal low-drag phenomena which may begin to unravel the origins of MDR. Intriguingly, these previous channel flow investigations observed hibernating turbulence in Newtonian (*i.e.* additive-free) fluid flow, which has hinted at the possibility of obtaining MDR without recourse to additives (*e.g.* in the boundary-layer flows over aircraft, submarines and around ships), by innovative flow control inducing or maintaining hibernating turbulence. However, before these types of control strategies could be applied, open questions remain: How frequently does Newtonian fluid flow enter a state of hibernation in turbulent boundary-layer flows? What are the time and spatial characteristics of hibernation in turbulent boundary-layer flows?

**Methods, Assumptions and Procedures**

Experiments were conducted in both an open-return wind tunnel and water flume at Newcastle University. The wind tunnel experiments were conducted at a free-stream velocity of $U_\infty = 6$ m/s where the free-stream turbulence intensity was around 0.5%. The turbulent boundary-layer flow was developed over a 3 m long flat plate which was installed in the lower half of a 457 x 457 mm$^2$ test section. The flow was tripped 100 mm downstream of an elliptic leading edge of the flat plate by a 3 mm high zig-zag trip[36]. The turbulent trip fixed the location of transition-to-turbulence and ensured a fully developed turbulent boundary-layer flow at all measurement locations. In the water flume, experiments were conducted at a free-stream velocity up to $U_\infty = 0.5$ m/s where the free-stream turbulence intensity was around 1%. The turbulent boundary-layer flow was developed over a 3 m glass plate, which formed the bottom of the 325 x 195 mm$^2$ (width x height) glass test section. Similar to the wind tunnel, the flow was tripped at the inlet of the test section with a 2 mm high zig-zag

trip to fix the transition point and ensure all measurements were acquired in a fully developed turbulent boundary-layer flow.

Throughout the report, $x$, $y$ and $z$ denote the streamwise, wall-normal and spanwise directions, and the symbols $U$, $V$ and $W$ indicate the instantaneous streamwise, wall-normal and spanwise velocities, respectively. The superscript $L$ indicate conditional sampling during low-drag intervals, the superscript + indicates the usual viscous scaling and an overbar indicates a time-averaged or an ensemble-averaged quantity. Fluctuating velocities are represented by lowercase symbols (e.g., $u$) and primed symbols (e.g., $u'$) denote r.m.s values of these fluctuations.

To detect the intervals of hibernating turbulence, Dantec 55R45 & 55R48 flush-mounted miniaturized hot-film probes were calibrated to measure the instantaneous wall-shear stress of the turbulent boundary-layer flow in air and water, respectively. The probes were powered and balanced by an IFA 100 anemometry system from TSI. The probes were operated in constant temperature mode with an overheat ratio of 1.8 (in air) and 1.08 (in water). Typically, a gain of 5 was applied to the voltage signal, which was low-pass filtered at 1 kHz prior to sampling. Once optimised by a square wave test, the probe had a typical frequency response on the order of 10's kHz. The 55R45 probe had a sensing element which was 0.2 mm long ($x^+ = xu_\tau/\nu = 3.6$ in the streamwise direction) and 0.75 mm wide ($z^+ = 13.5$ in the spanwise direction) and was flush mounted on the wall ($y = 0$ mm) at $x = 2.5$ m downstream of the turbulent trip in the wind tunnel. Here $u_\tau = (\tau_w/\rho)^{1/2}$ is the friction velocity at $Re_\tau = \delta u_\tau/\nu = 600$, $\tau_w$ is the wall-shear stress, $\rho$ is the fluid density, $\nu$ is the kinematic viscosity, and $\delta$ is the boundary-layer thickness. The 55R48 glue-on hot-film probe used in the water flume had a sensing element which was 0.1 mm long ($x^+ = 1.8$) and 0.9 mm wide ($z^+ = 16.2$) and was flush-mounted on the wall at $x = 2.35$ m downstream of the turbulent trip. Here the viscous scaling is shown for the highest friction Reynolds number of $Re_\tau = 880$.

The changes in turbulence structure during the intervals of hibernating turbulence were quantified by either Laser Doppler Velocimetry (LDV) or Stereoscopic Particle Image Velocimetry (SPIV). During the LDV measurements, the streamwise ($U$) and wall-normal ($V$) velocity components of the turbulent boundary layer were measured directly above the location of the hot-film probe at various wall-normal distances. The TSI LDV system consisted of two 1W solid state lasers with wavelengths of 514 nm and 488 nm, a TSI LDV probe, an XPD60 beam expander coupled with a beam displacer to allow Reynolds shear stress measurements from within the viscous sublayer, and a TLN15-480 lens, a 16-bit FSA-3500 burst spectrum analyser and a 3-axis traverse to permit autonomous profiling: see figure 1(a). The LDV system was operated in burst mode in conjunction with forward scatter optics in the wind tunnel and in backscatter in the water flume. The specially designed optical head provided a focal length of 480 mm and focused the laser beams to create a measurement volume with diameter of 0.0456 mm ($x^+ = 0.82$) and length of 0.3 mm ($z^+ = 5.4$) in the wind tunnel and water flume at the highest friction Reynolds number tested. A 4-channel, 12-bit, sample-and-hold analogue-to-digital converter (ADC), built into the FSA, was used to record the voltage signal outputted from the hot-film probe. The ADC was controlled by TSI FlowSizer software and sampled the devices when a Doppler burst was detected. This set-up ensured that the velocities and wall-shear stress were sampled simultaneously. In the wind tunnel, the air was seeded with nominal 1 μm diameter atomised olive oil generated by a TSI atomiser. In the water flume, silver coated glass hollow spheres with a nominal diameter of 10 μm were used to seed the flow. During experiments the air temperature in the wind tunnel was measured to an accuracy of ±0.04°C with an Omega PT100 powered by an Omega PT-104A DAQ module. The same temperature sensing system was using in the flume, which used an external recirculating chiller unit to keep the water at a constant value to within ±0.1°C.

During the SPIV measurements in the water flume, all three velocity components were measured in the spanwise-wall-normal ($z$-$y$) plane, directly above the location of the hot-film probe, with the oncoming flow moving through the laser light sheet: see figure 1(b). The LaVision high-speed SPIV system consisted of two Phantom VEO E-310L 1-megapixel high-speed cameras and a 15 mJ per pulse double cavity, 527 nm wavelength Litron LD15 YLF PIV laser. The SPIV measurements were taken 1.8 m downstream of the turbulent trip. The instantaneous wall-shear stress signal was time stamped alongside data collected by the SPIV system using a National Instruments Data Acquisition module. The instantaneous wall-shear stress signal was processed "on the fly", and once a low-drag event was detected, the SPIV data were downloaded for post-processing. Silver-coated glass hollow spheres with a nominal diameter of 10 μm were used to seed the flow. The SPIV data were obtained at friction Reynolds number of $Re_\tau = 335$, 650 and 880 with a field of view of 42 x 50 mm$^2$ ($y/\delta = 1$, $z/\delta = 1.2$). Images were acquired at a frequency of 1.2 kHz ($t^+ = tu_\tau^2/\upsilon = 0.3$) (single frame mode) at the highest friction Reynolds number. Data processing was performed using a recursive cross-correlation algorithm to generate velocity vectors over a 16 x 16-pixel interrogation area with 50% overlap, providing a spatial resolution of 0.92 x 0.92 mm$^2$ ($y^+ = 16.8$, $z^+ = 16.8$, at $Re_\tau = 880$).

Alfredsson *et al.*[37] showed that the thermal conductivity of a fluid can effect a hot-film probe's ability to measure fluctuating wall-shear stresses. Hot-film measurements in low thermal conductivity ($\lambda$) fluids, such as air ($\lambda = 0.024$ W/mK) or oil ($\lambda = 0.18$ W/mK), underestimated the wall-shear stress fluctuations by up to a factor of 4; however, measurements in water ($\lambda = 0.60$ W/mK) remained unaffected. The damping of the wall-shear

stress fluctuations was due to heat loss to the substrate, which was largest in air and smallest in water. In the previous channel flow experiments on hibernating turbulence,[23,24] the working fluid was a 60/40% concentration by weight of glycerine/water which had a thermal conductivity of $\lambda = 0.38$ W/mK. Whalley *et al*.[23] showed that the hot-film probe correctly captured the fluctuating wall-shear in this fluid medium by comparing probability density functions (PDFs) of the fluctuating wall-shear stress obtained with the flush-mounted hot-film probe and with LDV. Part of the current investigation was conducted in a wind tunnel. With a usual static calibration, figure 2(a), of the hot-film probe in either a laminar channel flow facility or by using LDV data from within the viscous sublayer[38] in the turbulent boundary-layer flow, the fluctuating wall-shear stresses obtained with the hot-film probe were underestimated; figure 2(c) shows the instantaneous wall-shear stress obtained with the flush-mounted hot-film probe (red line) and by an LDV probe (black line) which was positioned directly above the flush-mounted hot-film probe. To overcome the underestimation in the wall-shear stress fluctuations, a novel non-linear regression (NLR) calibration technique[39] has been used for the first time on flush-mounted hot-film probes to accurately measure the instantaneous wall-shear stress in air flows. The NLR calibration technique requires an independent measurement of the fluctuating wall-shear stress at a given Reynolds number. In the turbulent boundary-layer flow measurements, an LDV probe was positioned directly above the location of the flush-mounted hot-film probe within the viscous sublayer. Data was then acquired for several minutes with the hot-film probe and LDV probe so that the first 4 moments of the wall-shear stress signal can be obtained with the LDV data. Once the first 4 moments are known, an NLR algorithm was used to find the appropriate calibration coefficients for the hot-film probe to match the first 4 moments of the wall-shear signal acquired with the LDV. Figure 2(a) shows the NLR calibration curve (red line) alongside the usual statically calibrated response of the hot-film probe (black line). The NLR calibration curve is much broader, facilitating the capture of the full fluctuating wall-shear stress signal. The intersection of the two curves is the mean wall-shear stress, which both calibration techniques capture accurately. A comparison of the PDFs of the wall-shear signals generated with the two calibration techniques is shown in figure 2(b). The PDF of the statically calibrated hot-film probe (red cross) is narrow when compared to the PDF of the NLR calibrated hot-film probe (red circles). The PDF of the NLR calibrated hot-film probe collapses to the PDF obtained with LDV, which is a direct consequence of the NLR calibration procedure. The resulting instantaneous wall-shear stress signal from the NLR calibrated hot-film probe is shown in figure 2(d). Here, the wall-shear stress obtained with the hot-film probe (red line) closely matches the wall-shear stress obtained with LDV (black line) with a linear correlation coefficient of 0.83; note that the same data is shown in figure 2(c) with the statically calibrated hot-film probe for comparison. Any small differences between the two wall-shear stress signals are likely due to the experimental uncertainties between the two measurement techniques and contributions due to differences in the measurement control volumes. Interestingly, the linear correlation coefficient of the statically calibrated or NLR calibrated wall-shear signal when correlated with the LDV wall-shear signal is the same: the NLR calibration technique essentially amplifies the statically calibrated wall-shear signal by a constant factor across the full frequency spectrum to match onto the LDV wall-shear stress signal, at least for the Reynolds number studied here. This is likely a consequence of the third order polynomial calibration curves shown in figure 1(a) being approximately linear over the voltage range at these Reynolds numbers. The NLR calibration technique was used to calibrate the hot-film probes in both the wind tunnel and water flume investigations. The approach was used in the water flume as measurements were acquired at the highest friction Reynolds number in the facility. Therefore, a static calibration curve would have needed to be extrapolated to capture the fluctuations at that Reynolds number. The NLR calibration coefficients were compared to the coefficients from a static curve with data compared at lower Reynolds number to validate the NLR approach in the water flume.

**Results and Discussions**

Figure 3 (a) shows instantaneous and ensemble-averaged wall-shear stress signatures of the hibernating turbulence phenomena in a turbulent boundary-layer flow at $Re_\tau = 880$ in a water flume turbulent boundary later-flow. The wall-shear stress time series are captured using a flush-mounted hot-film probe calibrated using an NLR technique. The wall-shear stress data is post-processed using the criteria that a hibernating turbulence event is detected once the instantaneous wall-shear stress drops 10% below the mean wall-shear stress for a duration of $t^+ > 150$. Throughout figure 3, each hibernating turbulence event is aligned to begin at $t^+ = 0$, which is the point at which the instantaneous wall-shear stress initially drops 10% below the mean wall-shear stress. Each individual hibernating turbulence interval is shown by a thin grey line and the ensemble average through all instantaneous events is shown by the thick black line. The black dashed lines show the normalised mean wall-shear stress and the threshold line of 10% below the mean wall-shear stress. The red line and blue line show instantaneous hibernating turbulence events which last for a duration of $t^+ = 200$ and 300, respectively. The data presented in figure 3(a) was captured over a 6-hour window and shows 2732 independent hibernating turbulence events. The boundary layer hibernating turbulence signatures show remarkable resemblance to the hibernating turbulence events in transitional channel flows[23,24]. From an ensemble-averaged point of view, there

is a higher-than-average peak in wall-shear stress before the start of the hibernating turbulence interval, which is thought to be an artifact of conditionally sampling data[40], before falling to a plateau region starting from $t^+ > 25$.

The conditionally sampled and ensemble averaged wall-shear stress for a different wall-shear stress criterion and time criterion are shown in figure 3(b,c), respectively. Here, the more stringent the wall-shear stress criterion, for example, the detection of a hibernating turbulence event when the wall-shear stress drops to 20% (pink line) or 30% (black line) below the mean wall-shear stress for a duration of $t^+ > 150$ reduces the ensemble-averaged wall-shear stress in the plateau region, figure 3(c). Similarly, extending the time criterion so that a hibernating turbulence event is detected when the instantaneous wall-shear stress drops to 10% below the mean wall-shear stress for a duration of $t^+ > 150$ (green line), $t^+ > 200$ (pink line) and $t^+ > 250$ (black line) extends the plateau region, figure 3(c). Probability density functions (PDFs) of the wall-shear stress data at friction Reynolds numbers of $Re_\tau = 335$, 650 and 880 are shown in figure 3(d). Similarities with transitional channel flow data[23,24] can be seen, with PDFs of the entire time series appearing positive skewed and the PDFs of the low-drag data appearing symmetric. The choice of criterion used to detect the intervals of hibernating turbulence is critical, with intervals of longer duration and/or with lower stress occurring more infrequently: see figure 3(e,f), which shows the fraction of time spent in hibernation decreases exponentially as a function of time.

Conditionally sampled and ensemble-averaged streamwise velocity, wall-normal velocity and Reynolds shear stress during states of hibernating turbulence at $Re_\tau = 880$ are shown in figure 4. The grey thin lines show instantaneous events aligned to accentuate the evolution of velocities and Reynolds shear stress at the beginning of the hibernating turbulence intervals. In figure 4 (a), acquired at $y^+ = 18$, the thick black line shows an ensemble-average through all the instantaneous conditionally sampled data, the thick red line shows an instantaneous event with a duration of $t^+ > 200$ and the thick blue line shows an instantaneous event with a duration of $t^+ > 300$. A distinct difference is observed in the instantaneous evolution of the streamwise velocity and wall-shear stress signals. It was a condition when post-processing the wall-shear stress data that the signal remained below a threshold for a given duration. Yet conditionally sampling the streamwise velocity on the wall-shear stress data shows that instantaneous streamwise velocities fluctuate largely around the ensemble-averaged data: see the blue and red lines in figure 4(a). However, close to the wall, on an ensemble-averaged point of view, the streamwise velocity mimics the wall-shear stress signatures during the intervals of hibernating turbulence. There are small peaks at the start of the ensemble-averaged low-drag intervals, joined by a plateau of almost constant streamwise velocity. The coherence between the wall-shear stress and streamwise velocity is lost further away from the wall: see figure 5(a) which show ensemble-averaged data at various wall-normal distances. Instantaneous wall-normal velocity and Reynolds shear stress data at $y^+ = 18$ is shown in figure 4(b,c), respectively. Similar to the conditionally sampled streamwise velocity data, the instantaneous wall-normal velocity and Reynolds shear stress events fluctuate during states of hibernating turbulence. From an ensemble-averaged point of view, figure 5(b), there is a noticeable increase in averaged wall-normal velocity close to the wall. In contrast, there is a large reduction in ensemble-averaged Reynolds shear stress close to the wall at $y+ < 30$, figure 5(c). Beyond $y+ > 30$, there appears to be a slight increase during hibernation compared to the usual canonical data. Common across these three quantities is the reduction in fluctuation during the instantaneous events close to the wall at $y+ = 18$, which can be clearly seen in figure 4.

Figure 6 investigates the fluctuations across the streamwise and wall-normal velocities in more detail by plotting the joint PDFs of these quantities at $y^+ = 18$ ($Re_\tau = 880$). Figure 6 categorises the turbulent flow in the usual four quadrants[41], with the turbulent boundary layer having a higher probability of being in a state of ejection (low-speed fluid moving away from the wall, top left quadrant), or a state of sweep (high-speed fluid moving into the wall, bottom right quadrant): see figure 6(a). This situation changes significantly during hibernating turbulence, figure 6(b). During hibernating turbulence, there is a much higher probability that the wall-turbulent flow will be in a state of ejection, which can be clearly seen by the high density of data in the top left-hand quadrant. This would allow us to posit that the turbulence structure associated with hibernating turbulence may be a vortical flow system which is lifting low-speed fluid away from the near-wall region, similar to observations in transitional channel flow. What is also observed are instances of sweep-behaviour, which is perhaps in contrast to the sustained low-drag region associated with hibernating turbulence. As this data is a snapshot in time passing a small LDV probe away from the wall, these fluctuations may not be coherent enough to have made contact with the wall. The presence of sweep events in this region does indicate turbulence production, which points towards the flow behaviour in this region remaining somewhat chaotic even in these states of low drag.

Shown in figure 7 is the ensemble-averaged streamwise velocity plotted against wall-normal distance. The log-law is the black dot-dash line. The blue, red and pink closed symbols show the ensemble-averaged streamwise velocity measured during intervals of hibernating turbulence for various detection criteria in the wind tunnel, figure 7(a), at friction Reynolds numbers of $Re_\tau = 600$, and in the water flume, figure 7(b), at friction Reynolds numbers of $Re_\tau = 335$, 650 and 880. These data are averaged over the plateau region and are scaled with the ensemble-averaged wall-shear stress determined during the same time interval for LDV. Beyond $y^+ \approx 40$, the low-drag data appears to follow a gradient similar to the log-law, as observed with experiments[23,24]

and DNS[42] of hibernating turbulence in channel flows – the black solid circles are data taken from transitional channel flow experiments[24] at $Re_\tau = 70 – 100$, with a black line to guide the eye. There is remarkable collapse between the hibernating turbulence data acquired within the transitional channel flow and turbulent boundary-layer flow despite the boundary-layer flow data being acquired at a friction Reynolds number one order of magnitude larger than the channel flow data. A sensitivity analysis on the conditional sampling criteria shows that the conditionally-averaged streamwise velocity data is rather insensitive to small changes in the time criterion (blue closed symbols in figure 7(a)) used to detect hibernating turbulence. Here the conditionally-sampled streamwise velocity data collapses when using the criteria that hibernating turbulence occurs once the instantaneous wall-shear stress drops to 10% below the mean wall-shear stress for a duration of $t^+ > 150 – 400$. Making the wall-shear stress criterion more stringent, by conditionally sampling data once the instantaneous wall-shear stress drops to 70%, 75%, 80% or 85% below the mean wall-shear stress, causes a shift towards the MDR asymptote in the conditionally-sampled streamwise velocity data as shown in figure 7(a,b); these same trends have been observed in the recent experimental[24] and DNS[42] studies of hibernating turbulence in transitional channel flows. It should also be commented on that Dubief *et al*.[43] analysed the boundary-layer simulation data of Wu & Moin[44] to find that transitional boundary layers had intrinsic streamwise profiles which also approached the MDR asymptote. Further, Hutchins *et al.*[45] conditionally sampled streamwise velocity on low-drag events in a high Reynolds-number turbulent boundary-layer flow. They used the criterion that the flow enters into a state of low drag when the skin-friction fluctuation was below zero and observed an upward shift in the log-law rather than a change in log-law gradient as seen here up to the lower log-law region. This could be a consequence of Reynolds number as their study was conducted at $Re_\tau = 14200$, or that their conditional sampling technique did not have a stress/time criterion which may have caused the averaging out of the rare low-drag events observed here, and/or could also be due to the issues surrounding calibrating flush-mounted hot-film probes in air flows.

Figure 8 shows the turbulence intensity of hibernating turbulence in the turbulent boundary layer. When the data is scaled with the lower-than-average wall-shear stress, figure 8(a), both the streamwise and wall-normal turbulence intensities are increased above the usual canonical flow. In an absolute sense, when the data is scaled with the free-stream velocity, the streamwise turbulence intensity is markedly reduced over the entire boundary layer, compared to the canonical data, as observed in the instantaneous data shown in figure 4(a). The wall-normal intensity sightly reduces when $y^+ > 100$.

The Reynold shear stress data during intervals of hibernation is shown in figure 9, scaled with the lower-than-average wall-shear stress in figure 9(a) then free-stream velocity in figure 9(b). When these data are scaled with the lower-than-average wall-shear stress, the Reynolds shear stress is largely increased throughout the boundary layer, due to the scaling with the low wall-shear stress. When scaled with free-stream velocity, the Reynolds shear stress is reduced close to the wall, $y^+ < 30$, before rising to the levels associated with its canonical counterpart up to $y+ = 60$, after which the Reynolds shear stress reduces throughout the remainder of the boundary-layer thickness. The outer scaling helps to illustrate that hibernating turbulence is associated with much lower turbulence production compared to the fuller canonical footprint of wall-turbulence at the same global Reynolds number.

To elucidate on the distributions of streamwise velocity during hibernating turbulence, PDFs of the instantaneous streamwise velocity scaled with the instantaneous wall-shear stress is shown in figure 10 at $y^+ = 27$, $y^+ = 37$ and $y^+ = 66$ in a turbulent boundary layer at a friction Reynolds number of $Re_\tau = 880$. Plotting the entire canonical data (black solid lines) at these locations shows, from an instantaneous point of view, that the flow spends some portion of time above and below the MDR asymptote and classical log-law, less so beyond the MDR asymptote with increasing distance from the wall. Conditionally sampling these data to separate the hibernating turbulence data (blue solid lines) shows that during intervals of low drag, the fluid flow spends some part of its trajectory around and below the Prandtl–von Kármán log-law as well as beyond the MDR asymptote. These PDF plots support an analogy to dynamic systems theory[14], where it's been shown in transitional channel flows, that the flow predominantly resides around the Prandtl-von Kármán log-law, then takes a rare excursion towards a low-energetic, or low-drag state, close to the MDR asymptote. From an ensemble-averaged point of view, these relatively low-Reynolds number turbulent boundary layer flows appear to be somewhat bounded between the Prandtl-von Kármán log-law and the MDR asymptote.

Finally, a typical instantaneous snapshot of the streamwise velocity during a hibernating turbulence event, captured with SPIV at $Re_\tau = 880$, is shown in figure 11(a). At times during the low-drag event, a counter-rotating vortex pair meanders in the spanwise direction lifting low-speed fluid from the near-wall region throughout the height of the boundary layer, similar to an ejection event: see figure 6(b). The ensemble-averaged streamwise velocity throughout the 460 hibernating turbulence events captured with SPIV is shown in figure 11(b). From an averaged point of view, the hibernating turbulence flow structure is characterized by a low-stress streak which is flanked by a quasi-streamwise vortex; this is in excellent agreement with previous transitional channel flow investigations[23,24,42]. Figure 11(c) shows streamwise velocity fluctuation in the $(x^+, z^+)$ plane at $y^+ = 28$. This figure has been generated by using Taylor's hypothesis[46] on the SPIV data using the local

mean streamwise velocity as the convection speed. Here a streamwise-orientated low-speed streak meanders in the spanwise direction around $z^+ = 0$, the location of the wall-shear stress sensor. The low-speed, and stress, region is flanked on either side by regions of high streamwise velocity fluctuation, perhaps indicative of the downwash regions associated with the quasi-streamwise vortices which characterise the hibernating turbulence phenomena.

**Conclusions**

Hibernating turbulence has been successfully detected and characterised in turbulent boundary-layer flows at friction Reynolds numbers up to $Re_\tau = 880$. The hibernating turbulence detected in the turbulent boundary layer shows strong resemblance to earlier work in transitional channel flows. The hibernating turbulence is characterised by a low-stress, low-speed streak, which is flanked on either side by regions of higher-than-average streamwise velocity, generated by weak quasi-streamwise vortical flow structures whose legs extend towards the wall to create the low-speed streaky structure of hibernating turbulence. Whilst hibernating turbulence is characterised by states of low drag, the vortical flow structures associated with hibernating turbulence remain chaotic in nature, meandering in the spanwise direction as they convect downstream, but generate only small amounts of turbulence themselves. The hibernating turbulence events occur randomly in space and in time in the turbulent boundary-layer flow, with these intrinsic events generating local skin-friction drag values up to 75% lower than the time-averaged mean skin friction. However, these hibernating turbulence events are rare, typically being found in a single location less than 10% of the time depending on the conditional sampling criteria. It has been shown that the ensemble-averaged streamwise velocity during intervals of hibernating turbulence approaches the MDR asymptote up to $y^+ = 40$, in excellent agreement with previous experiments and DNS on transitional channel flow. Further from the wall, the ensemble-averaged streamwise velocity profile follows a gradient similar to the classical Prandtl-von Kármán log-law but upshifted due to scaling with the lower-than-average wall-shear stress, suggesting that the fluid flow loses communication with the wall. Analysing the time-trajectories of the streamwise velocity during hibernating turbulence has shown that there are times when the turbulent boundary-layer flow will move beyond the MDR asymptote, and also beyond the Prandtl-von Kármán log-law too, even when the ensemble-averaged streamwise velocity appears to have fallen away from the MDR asymptote. A dynamical systems description of the turbulent boundary layer is useful with regards to hibernating turbulence. The turbulent boundary layer spends a large proportion of its time close to the classical Prandtl-von Kármán log-law, but on rare occasions takes an excursion towards a laminar attractor, the MDR asymptote. Perhaps more broadly, the dynamics of the turbulent boundary could be said to be enveloped somewhere between the classical von-Kármán log-law and the MDR asymptote.

**Acknowledgements**

This work has been conducted by Dr Tao Lui and Mr Aryan Moody, with technical support provided by Mr Michael Wilkes, under the supervision of Dr Richard Whalley and Dr David Swailes.

**References**

1. Robinson, S. K. Coherent motions in the turbulent boundary layer. *Ann Rev Fluid Mech* **23**, (1991).

2. Kline, S. J., Reynolds, W. C., Schraub, F. A. & Runstadler, P. W. The structure of turbulent boundary layers. *J Fluid Mech* **30**, (1967).

3. Head, M. R. & Bandyopadhyay, P. New aspects of turbulent boundary layer structure. *J Fluid Mech* **107**, (1981).

4. Hutchins, N., Hambleton, W. T. & Marusic, I. Inclined cross-stream stereo particle image velocimetry measurements in turbulent boundary layers. *J Fluid Mech* **541**, (2005).

5. Adrian, R. Hairpin vortex organisation in wall turbulence. *Phys. Fluids* **19**, (2007).

6. Karniadakis, G. E. & Choi, K. S. Mechanisms on transverse motions in turbulent wall flows. *Ann Rev Fluid Mech* **35**, (2003).

7. Choi, K. S. Near-wall structure of a turbulent boundary layer with riblets. *J Fluid Mech* **208**, (1989).

8. Garcia-Mayoral, R. & Jimenez, J. Drag reduction by riblets. *Philos Trans R Soc A* **369**, (2011).

9. O'Connor, J. *et al.* Optimisation and Analysis of Streamwise-Varying Wall-Normal Blowing in a Turbulent Boundary Layer. *Flow Turbul Combust* **110**, 993–1021 (2023).

10. Diessner, M. *et al.* Investigating Bayesian optimization for expensive-to-evaluate black box functions: Application in fluid dynamics. *Front Appl Math Stat* **8**, (2022).

11. Whalley, R. D. & Choi, K. S. Turbulent boundary-layer control with plasma spanwise travelling waves. *Exp Fluids* **55**, (2014).

12. Choi, K. S., Jukes, T. N. & Whalley, R. D. Turbulent boundary-layer control with plasma actuators. *Philos Trans R Soc A* **369**, (2011).

13. Quadrio, M. Drag reduction in turbulent boundary layers by in-plane wall motion. *Philos Trans R Soc A* **369**, (2011).

14. Graham, M. D. Drag reduction and the dynamics of turbulence in simple and complex fluids. *Phys Fluids* **26**, (2014).

15. Virk, P. S. Drag reduction fundamentals. *AIChE J* **21**, (1975).

16. Owolabi, B. E., Dennis, D. J. C. & Poole, R. J. Turbulent drag reduction by polymer additives in parallel-shear flows. *J Fluid Mech* **827**, (2017).

17. Xi, L. & Graham, M. D. Intermittent dynamics of turbulence hibernation in Newtonian and viscoelastic minimal channel flows. *J Fluid Mech* **693**, (2012).

18. Xi, L. & Graham, M. D. Dynamics on the laminar-turbulent boundary and the origin of the maximum drag reduction asymptote. *Phys Rev Lett* **108**, (2012).

19. Xi, L. & Graham, M. D. Turbulent drag reduction and multistage transitions in viscoelastic minimal flow units. *J Fluid Mech* **647**, (2010).

20. Xi, L. & Graham, M. D. Active and hibernating turbulence in minimal channel flow of Newtonian and polymeric fluids. *Phys Rev Lett* **104**, (2010).

21. Wang, S. N., Shekar, A. & Graham, M. D. Spatiotemporal dynamics of viscoelastic turbulence in transitional channel flow. *J Non Newt Fluid Mech* **244**, (2017).

22. Jimenez, J. & Moin, P. The minimal flow unit in near-wall turbulence. *J Fluid Mech* **225**, (1991).

23. Whalley, R. D. *et al.* Low-drag events in transitional wall-bounded turbulence. *Phys Rev Fluids* **2**, (2017).

24. Whalley, R. D., Dennis, D. J. C., Graham, M. D. & Poole, R. J. An experimental investigation into spatiotemporal intermittencies in turbulent channel flow close to transition. *Exp Fluids* **60**, 102 (2019).

25. Park, J. S. & Graham, M. D. Exact coherent states and connections to turbulent dynamics in minimal channel flow. *J Fluid Mech* **782**, (2015).

26. Hof, B. *et al.* Experimental observations of nonlinear traveling waves in turbulent pipe flow. *Science (1979)* **305**, (2004).

27. Kerswell, R. R. Recent progress in understanding the transition in pipe flow. *Nonlinearity* **18**, (2005).

28. Eckhardt, B., Schnieder, T. M., Hof, B. & Westerweel, J. Turbulence transition in pipe flow. *Ann Rev Fluid Mech* **39**, (2007).

29. Willis, A. P., Peixinho, J., Kerswell, R. R. & Mullin, T. Experimental and theoretical progress in pipe flow transition. *Philos Trans R Soc A* **366**, (2008).

30. Kawahara, G., Uhlmann, M. & Veen, L. The significance of simple invariant solutions in turbulent flows. *Ann Rev Fluid Mech* **44**, (2012).

31. Waleffe, F. Homotopy of exact coherent structures in plane shear flows. *Phys Fluids* **15**, (2003).

32. Wedin, H. & Kerswell, R. R. Exact coherent structures in pipe flow: travelling wave solutions. *J Fluid Mech* **508**, (2004).

33. Eckhardt, B., Faisst, H., Schmiegel, A. & Schneider, T. M. Dynamical systems and the transition to turbulence in linearly stable shear flows. *Philos Trans R Soc A* **366**, (2008).

34. Gibson, J. F., Halcrow, J. & Cvitanovic, P. Visualizing the geometry of state space in plane couette flow. *J Fluid Mech* **611**, (2008).

35. Waleffe, F. Three-dimensional coherent states in plane shear flows. *Phys Rev Lett* **81**, (1998).

36. Elsinga, G. E. & Westerweel, J. Tomographic-PIV measurement of the flow around a zigzag boundary layer trip. *Exp Fluids* **52**, 865–876 (2012).

37. Alfredsson, P. H., Johansson, A. V, Haritonidid, J. H. & Eckelmann, H. The fluctuating wall-shear stress and the velocity field in the viscous sublayer. *Phys Fluids* **31**, (1988).

38. Hutchins, N. & Choi, K. S. Accurate measurements of local skin friction coefficient using hot-wire anemometry. *Prog Aerosp Sci* **38**, (2002).

39. Agrawal, R., Whalley, R. D., Ng, H. C.-H., Dennis, D. J. C. & Poole, R. J. Minimizing recalibration using a non-linear regression technique for thermal anemometry. *Exp Fluids* **60**, 116 (2019).

40. Agrawal, R. *et al.* Low- and High-Drag Intermittencies in Turbulent Channel Flows. *Entropy* **22**, 1126 (2020).

41. Willmarth, W. W. & Lu, S. S. Structure of the Reynolds stress near the wall. *J Fluid Mech* **55**, 65–92 (1972).

42. Kushwaha, A., Park, J. S. & Graham, M. D. Temporal and spatial intermittencies within channel flow turbulence near transition. *Phys Rev Fluids* **2**, (2017).

43. Dubief, Y., White, C. M., Shaqfeh, E. S. G. & Terrapon, V. E. Polymer maximum drag reduction: A unique transitional state. *Centre for Turbulence Briefs* 395–404 (2010).

44. Wu, X. & Moin, P. Direct numerical simulation of turbulence in a nominally zero-pressure-gradient flat-plate boundary layer. *J Fluid Mech* **630**, 5–41 (2009).

45. Hutchins, N., Monty, J. P., Ganapathisubramani, B., Ng, H. C. H. & Marusic, I. Three-dimensional conditional structure of a high-Reynolds-number turbulent boundary layer. *J Fluid Mech* **673**, (2011).

46. Dennis, D. J. C. & Nickels, T. B. On the limitations of Taylor's hypothesis in constructing long structures in a turbulent boundary layer. *J Fluid Mech* **614**, 197–206 (2008).

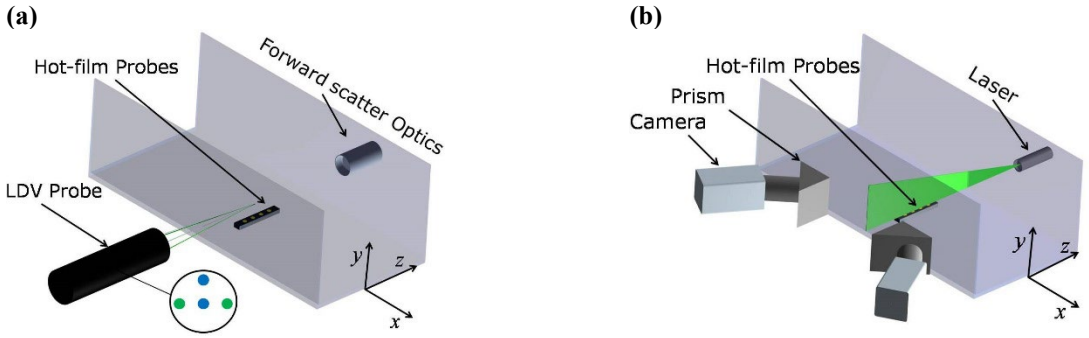


**Figure 1: (a) Schematic of the 2D LDV measurements, (b) stereoscopic PIV measurements in the *y*-*z* plane.**

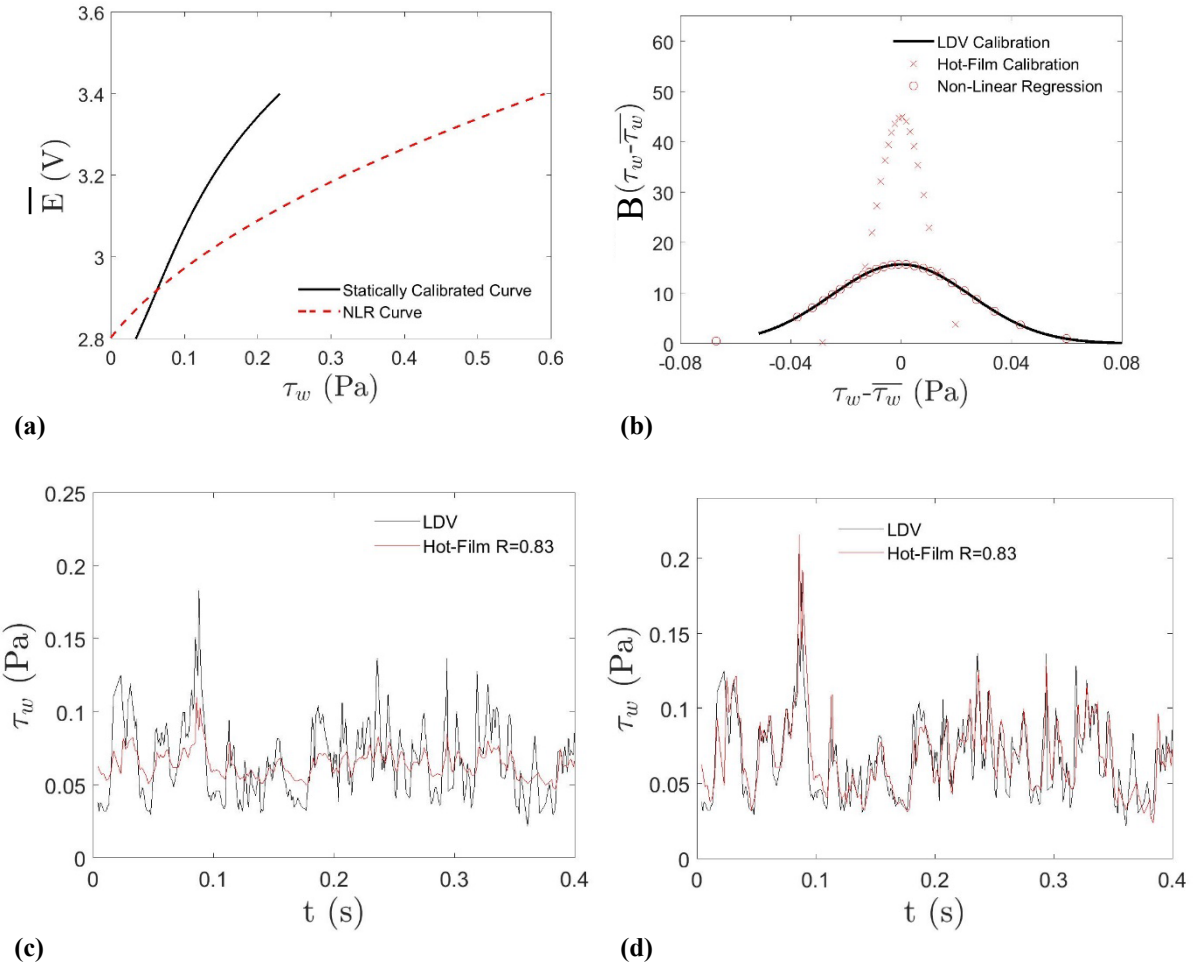


**Figure 2: (a) Calibration curves for the flush-mounted hot-film probe using a standard statically calibrated approach (black line) and a non-linear-regression (NLR) approach, (b) probability density functions (PDFs) of the fluctuating wall-shear stress obtained via static calibration (red cross), NLR (red circle) and with laser Doppler velocimetry (LDV, black line), (c) an example of instantaneous wall-shear obtained with LDV (black line) directly above the location of the hot-film probe (red line) which is processed with a static calibration and (d) an example of instantaneous wall-shear obtained with LDV (black line) directly above the location of the hot-film probe (red line) which is processed with an NLR calibration technique.**

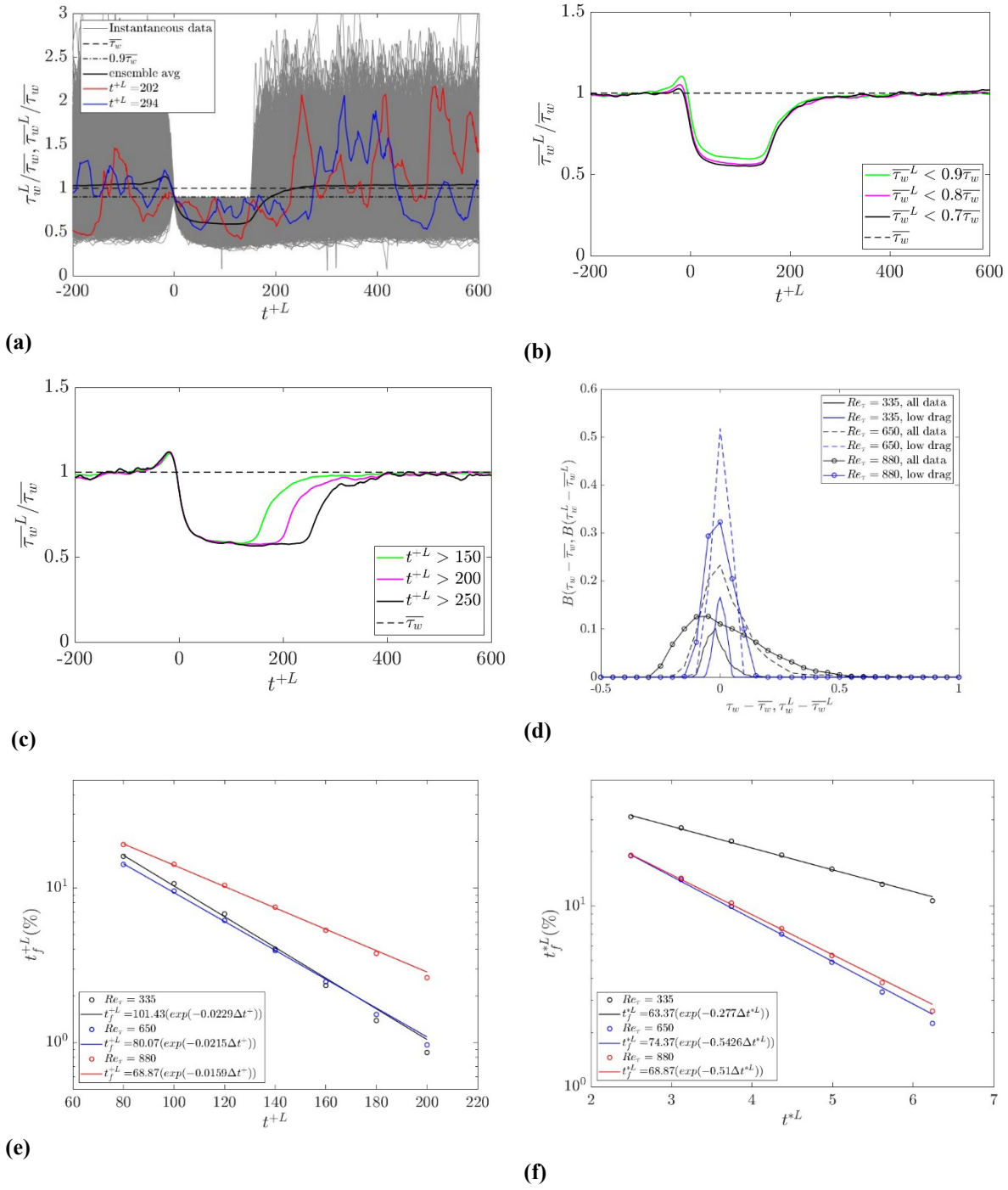


**Figure 3: (a) Instantaneous (grey thin lines) and ensemble-averaged wall-shear stress signatures (black thick lines) of hibernating turbulence in a turbulent boundary-layer flow at $Re_\tau = 880$ in a water flume. The red line and blue lines show instantaneous hibernating turbulence events which last for a duration of $t^+ = 200$ and 300, respectively. (b) Ensemble-averaged wall-shear stress signatures using the criterion that events are detected with duration of $t^+ > 150$ when the instantaneous wall-shear stress remains 10% below the mean wall-shear stress (green line), 20% below the mean wall-shear stress (pink line) and 30% below the mean wall-shear stress (black line). (c) Ensemble-averaged wall-shear stress signatures using the criterion that hibernation is detected when the instantaneous wall-shear stress drops 10% below the mean wall-shear stress for a duration of $t^+ > 150$ (green line), $t^+ > 200$ (pink line) and $t^+ > 250$ (black line). (d) PDFs of wall-shear stress fluctuation during hibernation, 10% below the mean wall-shear stress for a duration of $t^+ > 150$, for $Re_\tau = 335$ (solid lines), 650 (dashed lines) and 880 (open circles), alongside canonical date. (e,f) Fraction of time spent in hibernation when the wall-shear stress falls 10% below the mean in (e) inner and (f) outer scaling. All data acquired in a turbulent boundary layer in a water flume.**

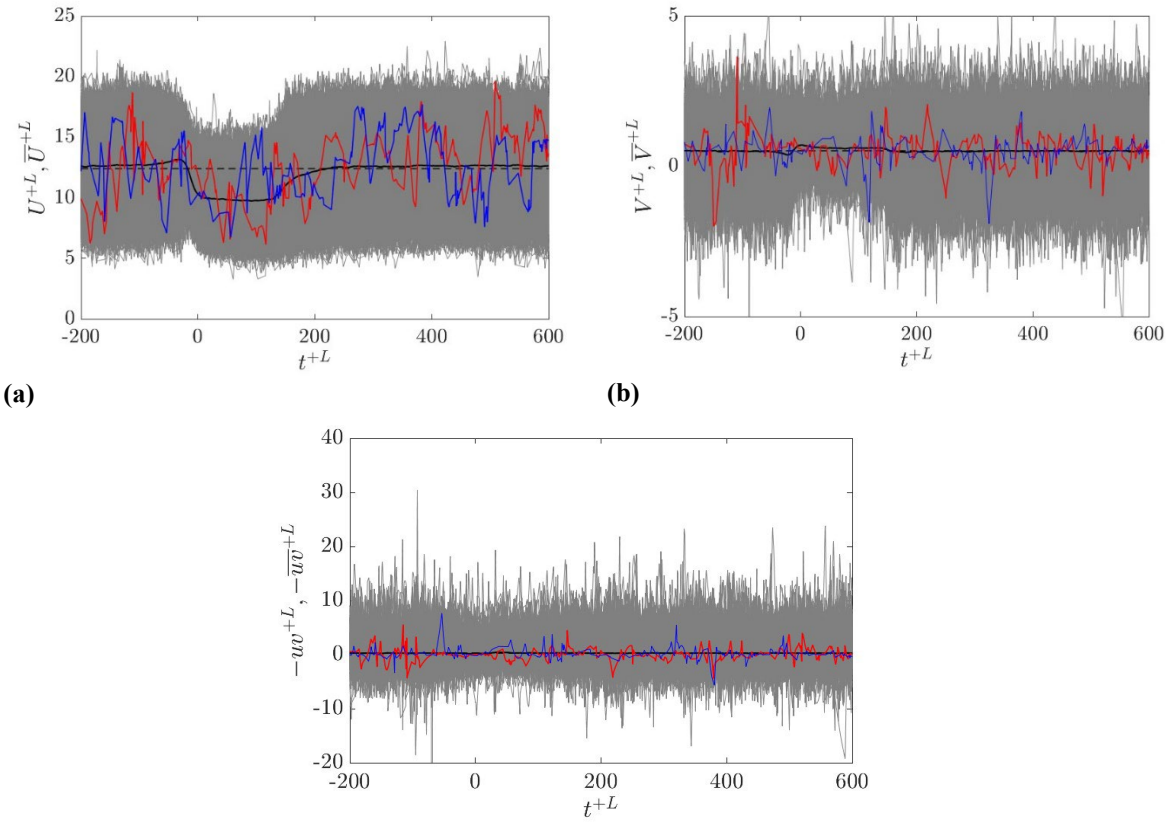


**Figure 4: Conditionally sampled instantaneous (grey thin lines) and conditionally sampled and ensemble-averaged (thick black line) (a) streamwise velocity, (b) wall-normal velocity and (c) Reynolds shear stress during intervals of hibernating turbulence at $y^+ = 18$ at $Re_\tau = 880$ in a water flume turbulent boundary layer. The red line and blue line show conditionally sampled instantaneous hibernating turbulence events which last for a duration of $t^+ > 200$ and 300, respectively. All data is processed using the criterion that the flow enters a state of hibernating turbulence when the instantaneous wall-shear stress falls 10% below the mean wall-shear stress for $t^+ > 150$. Shown are 2700 events detected over a period of 6 hours.**

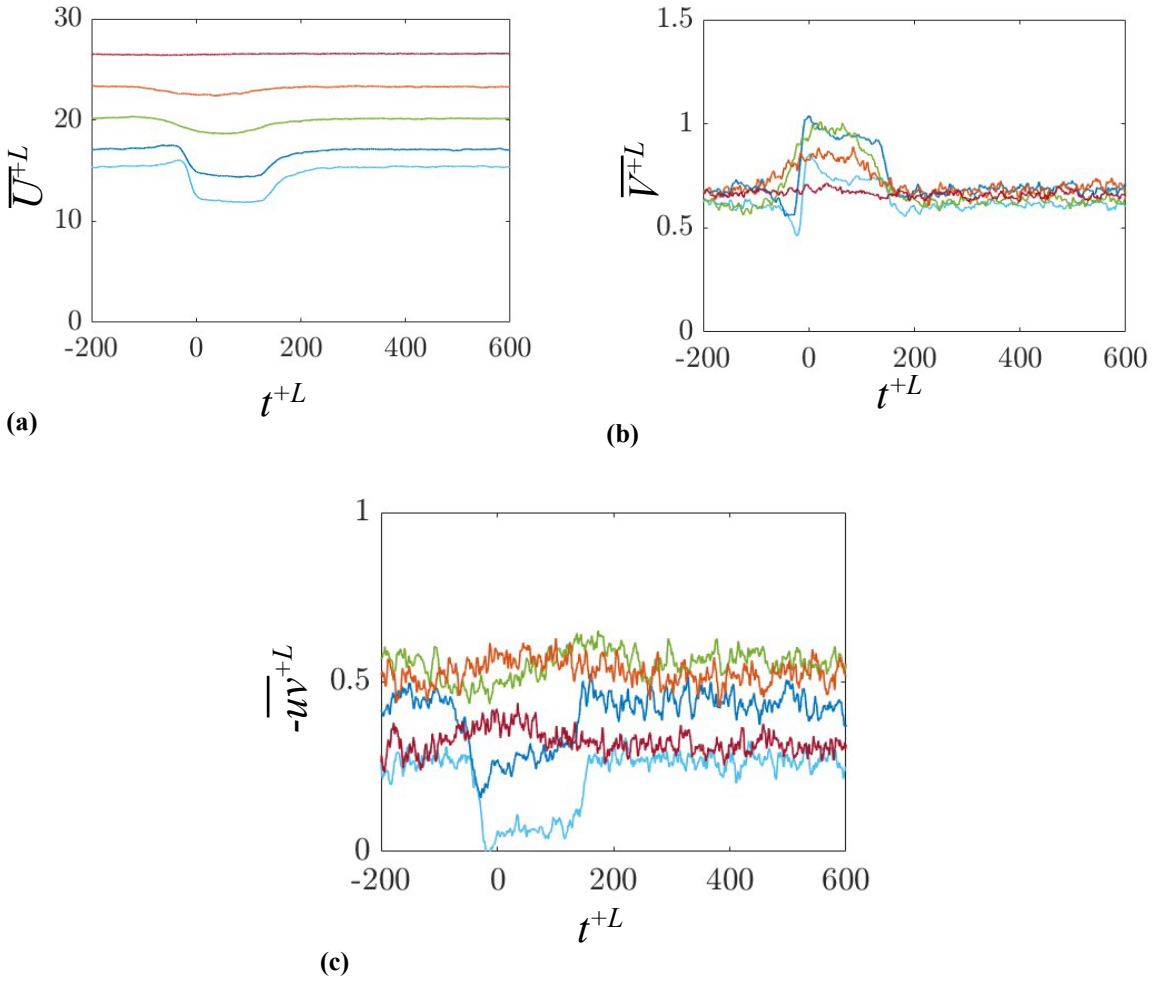


**Figure 5: Conditionally sampled and ensemble-averaged (a) streamwise velocity, (b) wall-normal velocity and (c) Reynolds shear stress during intervals of hibernating turbulence at $y^+ = 18$ (light blue line, 2732 events), $y^+ = 27$ (dark blue line, 3070 events), $y^+ = 103$ (green line, 4246 events), $y^+ = 262$ (orange line, 2486 events), $y^+ = 661$ (red line, 1670 events) in a water flume boundary layer at $Re_\tau = 880$. All data is processed using the criterion that the flow enters a state of hibernating turbulence when the instantaneous wall-shear stress falls 10% below the mean wall-shear stress for $t^+ > 150$.**

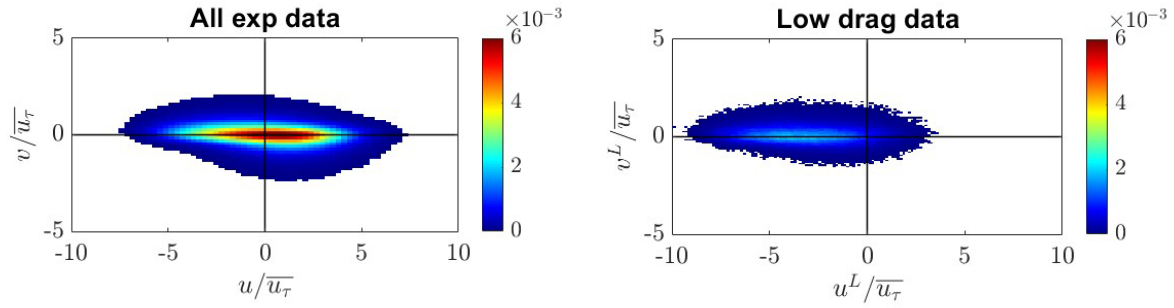


**Figure 6: Joint PDFs of streamwise and wall-normal velocity fluctuations for (a) canonical data and (b) conditionally sampled low-drag data at $y^+ = 18$ for $Re_\tau = 880$ in a water flume turbulent boundary layer. Data normalised by time-averaged friction velocity.**

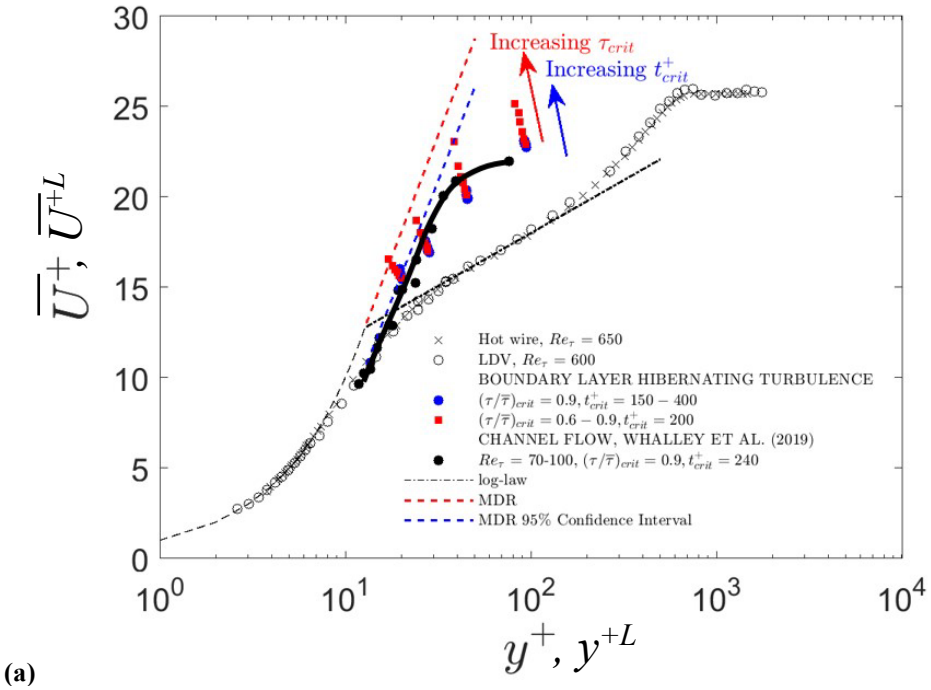


**(a)**

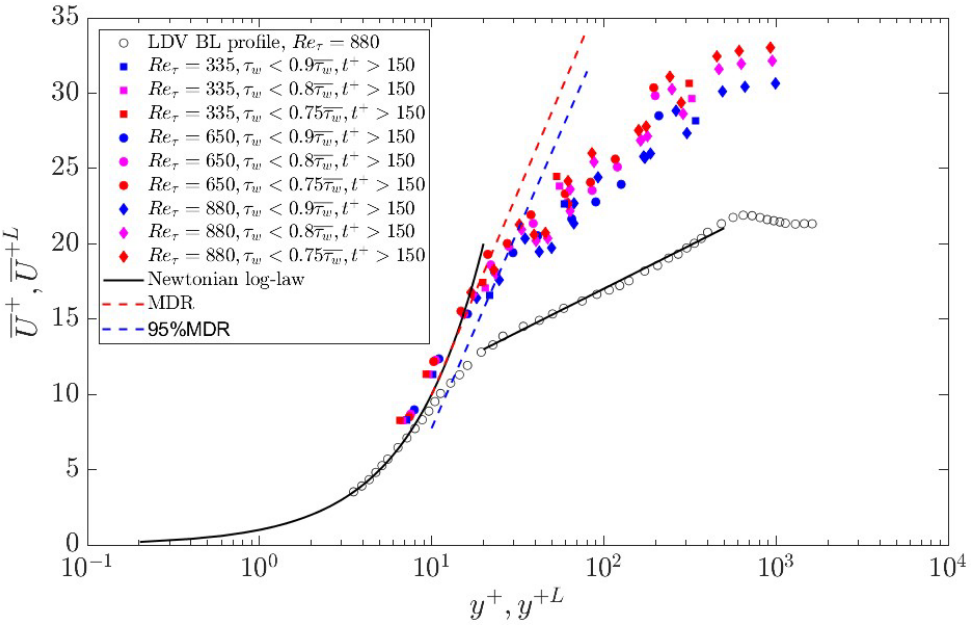


**(b)**

**Figure 7: Conditionally averaged streamwise velocity scaled with conditionally averaged wall-shear stress at (a) $Re_\tau = 600$ in a wind tunnel and at (b) $Re_\tau = 335$, 650 and 880 in a water flume. A sensitivity analysis on the conditional sampling criteria show conditionally averaged streamwise velocity data in (a) when using the criteria that the flow enters into a state of hibernating once the instantaneous wall-shear stress drops between 10 – 30% below the mean wall-shear stress for a duration of $t^+ > 200$ (red closed symbols), and once the instantaneous wall-shear stress drops 10% below the mean wall-shear stress for a duration of $t^+ > 200 – 400$ (blue closed symbols). In (b) as legend states. The open symbols show the usual time-averaged streamwise velocity acquired with hot-wire anemometry (black cross) and LDV (black circles). The red dashed line shows the MDR asymptote and the blue dashed lines shows the 95% confidence interval to the MDR asymptote. The black solid/dot-dash line is the law of the wall. For comparison the channel flow data from Whalley *et al.*[23] taken at $Re_\tau = 70 – 100$ is shown by the black closed symbols with a black line to guide the eye in (a).**

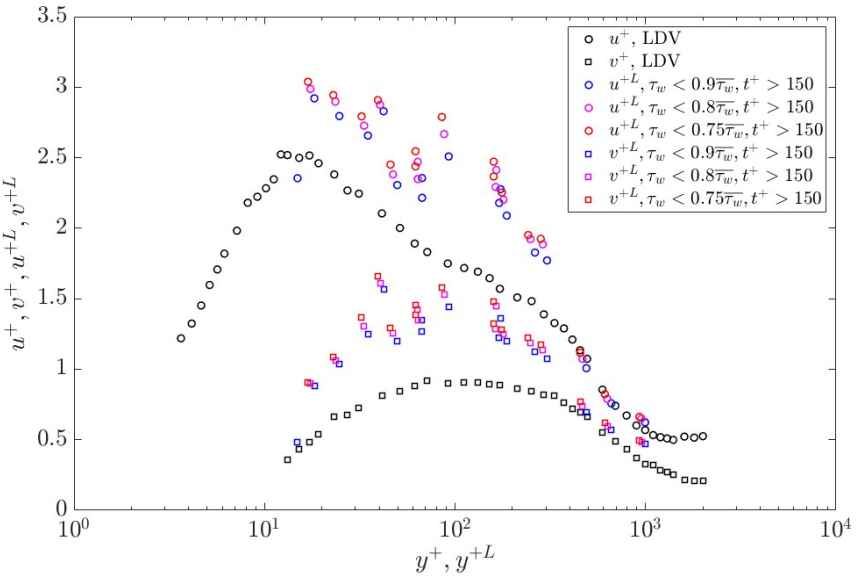


**(a)**

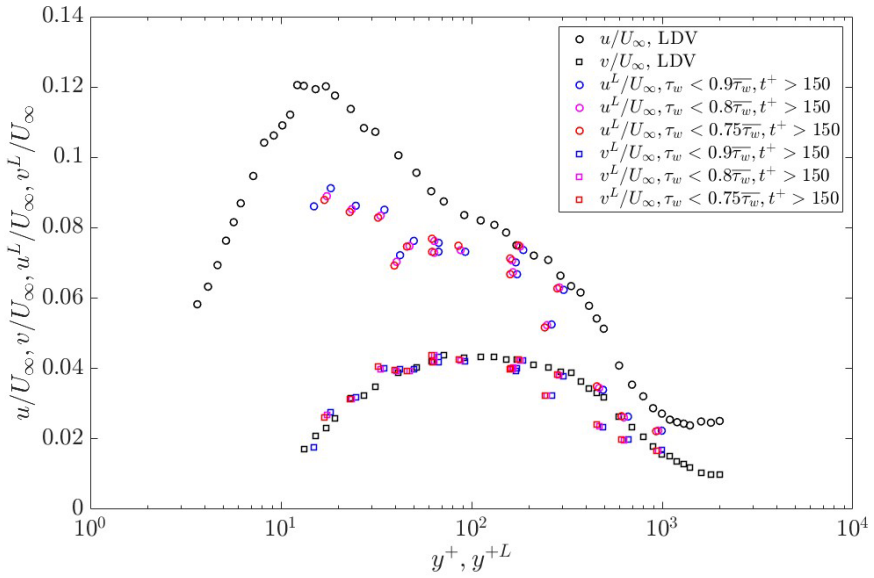


**(b)**

**Figure 8: Conditionally averaged streamwise and wall-normal turbulence intensity during intervals of hibernating turbulence with (a) inner scaling and (b) outer scaling. Data acquired in a water flume turbulent boundary layer at $Re_\tau = 880$.**

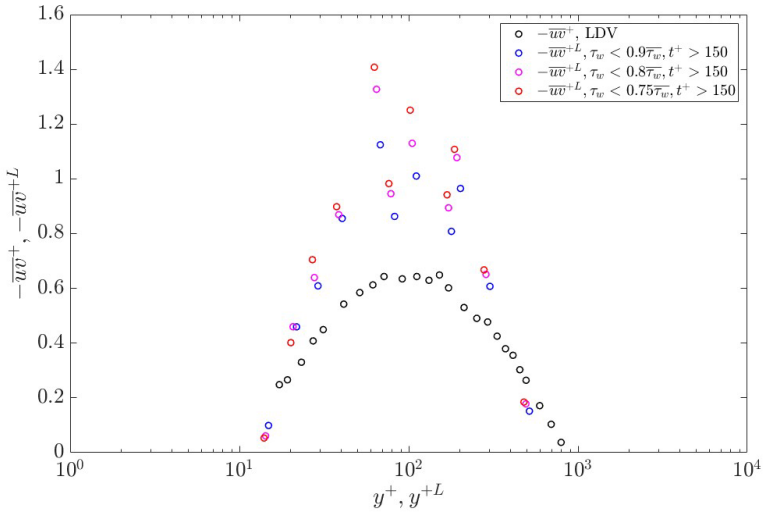


**(a)**

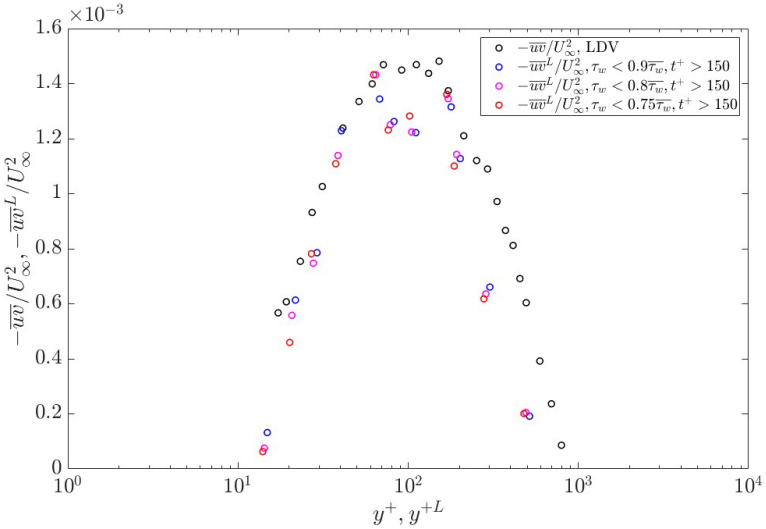


**(b)**

**Figure 9: Conditionally averaged Reynolds shear stress during intervals of hibernating turbulence with (a) inner scaling and (b) outer scaling. Data acquired in a water flume turbulent boundary layer at $Re_\tau = 880$.**

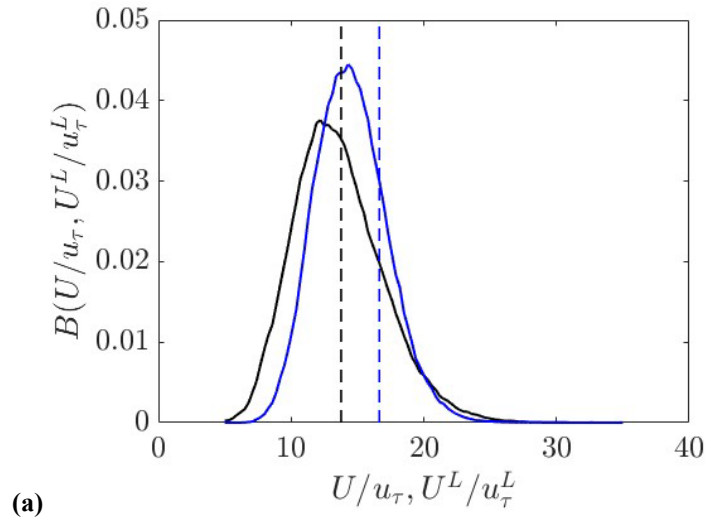


**(a)**

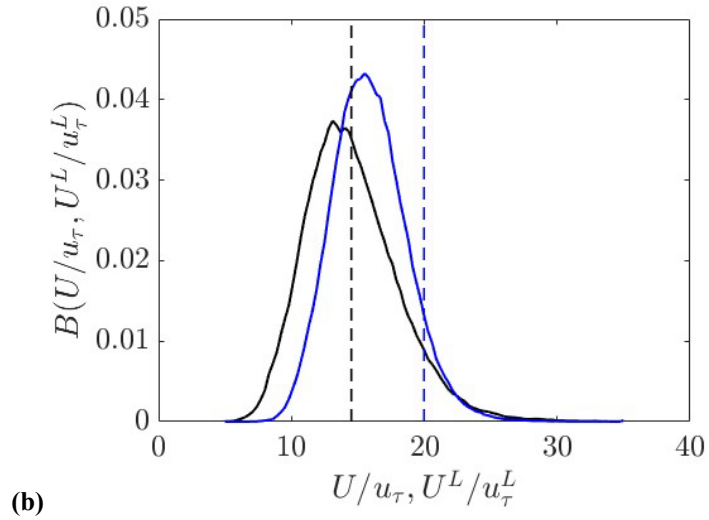


**(b)**

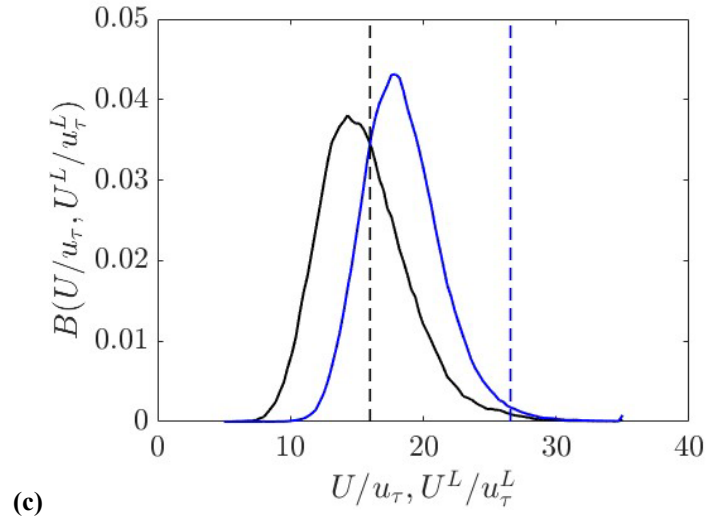


**(c)**

**Figure 10: PDFs of conditionally sampled instantaneous streamwise velocity scaled with instantaneous wall shear stress during low-drag events (blue solid line), alongside PDFs of all data (black solid line) scaled with instantaneous wall shear stress at (a) $y^+ = 27$, (b) $y^+ = 37$ and (c) $y^+ = 66$. The black dashed line shows the location of the Prandtl–von Kármán log-law and the blue dashed line shows the location of the 95% confidence interval of the MDR asymptote[14,15].**

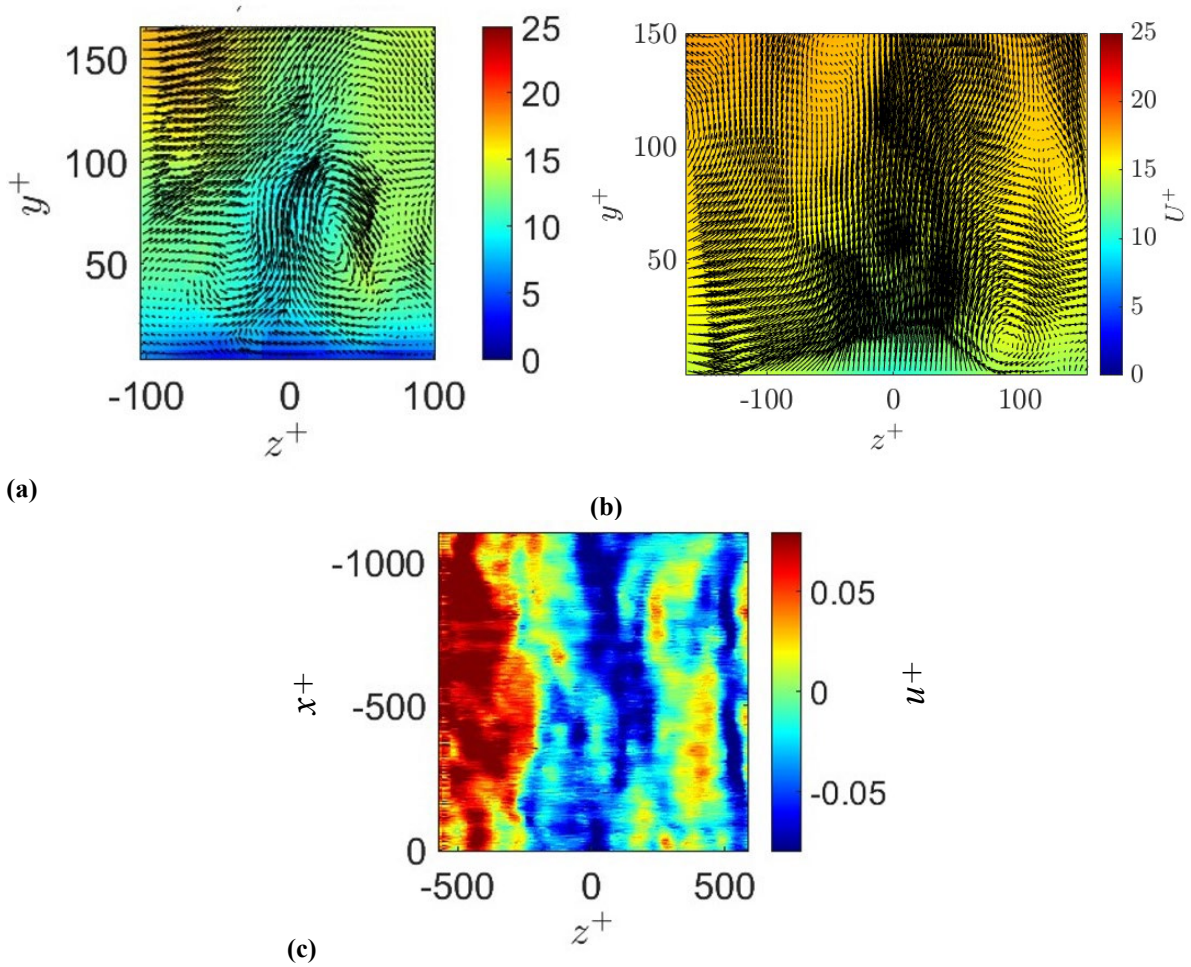


**Figure 11: (a) Instantaneous and (b) ensemble-averaged streamwise velocity scaled with time-averaged wall shear stress at $Re_\tau$ = 880 during hibernating turbulence captured using SPIV. The ensemble-average comprises 460 SPIV snapshots acquired over a single hibernating turbulence event. Black arrows show wall-normal and spanwise velocities. The ($y^+$,$z^+$) axes are scaled with the time-averaged wall shear stress. (c) Shows a projection of the streamwise velocity fluctuation acquired with SPIV into the ($x$+, $z$+) plane using Taylor's hypothesis at $y^+$ = 28.**

**PhD Student:**
Mr Aryan Moody

**Postdoctoral Researcher:**
Dr Tao Liu

**Journal Articles:**
Mahfoze OA, Moody A, Wynn A, Whalley RD, Laizet S. Reducing the skin-friction drag of a turbulent boundary-layer flow with low-amplitude wall-normal blowing within a Bayesian optimization framework. Physical Review Fluids 2019, 4(9), 094601.

**Conference Papers/Talks:**

Liu T, Wilkes M, Swailes DC, Whalley RD. (2023). Measurements of coherent structures during low-drag hibernation events in turbulent boundary-layer flows. In: 76th Annual Meeting of the Division of Fluid Dynamics, Washington.

Liu T, Wilkes M, Swailes DC, Whalley RD. (2023). Detection and characterisation of hibernating turbulence in boundary-layer flows. In: UK Fluids Conference, Glasgow, UK.

Liu T, Wilkes M, Swailes DC, Whalley RD. (2023). On the detection and characterisation of intermittent low-drag behaviour in turbulent boundary-layer flows. In: 18th European Turbulence Conference, Valencia, Spain.

Liu T, Moody A, Wilkes M, Swailes DC, Whalley RD. (2022). On the detection and characterisation of hibernating turbulence in boundary-layer flows. *In: European Drag Reduction and Flow Control Meeting, Paris*, France.

Mahfoze OA, Moody A, Wynn A, Whalley RD, Laizet S. (2020). Bayesian optimisation of intermittent wall blowing in a turbulent boundary layer for net power saving. *In: UK Fluids Network SIG on turbulent skin-friction drag reduction*, City University of London, UK.

Mahfoze OA, Moody A, Wynn A, Whalley RD, Laizet S. (2019). Bayesian optimisation of intermittent wall blowing in a turbulent boundary layer for net power saving. *In: 11th International Symposium on Turbulence and Shear Flow Phenomena*, University of Southampton, UK.

Mahfoze OA, Moody A, Wynn A, Whalley RD, Laizet S. (2019). Bayesian optimisation of intermittent wall blowing in a turbulent boundary layer for net power saving. *In: UK Fluids Network SIG on turbulent skin-friction drag reduction*, Cambridge University, UK.

Mahfoze OA, Moody A, Wynn A, Whalley, RD, Laizet S. (2019). Bayesian optimisation of wall blowing to control energy and skin friction in a turbulent boundary layer. *In: European Drag Reduction and Flow Control Meeting*, Bad Herrenalb, Germany.

**Invited Seminars:**
Whalley RD. (2020). Detecting low-drag events in turbulent boundary-layer flows. *Imperial College London*, UK (invited).

Whalley RD. (2020). Overview: Hibernating turbulence, MEMS wall-shear stress sensors and turbulent skin-friction drag reduction. *UK Fluids SIG on turbulent skin-friction drag reduction, City University of London*, UK.

Whalley RD. (2018). Spatiotemporal intermittencies in turbulent channel flow close to transition. *UK Fluids Network SIG on non-equilibrium turbulence, Imperial College London,* UK (invited).